Supplementary Information

Single-Atom Electronic Bridges Facilitate Cascade Electron Transfer from Encapsulated Polyoxometalates to Metal-Organic Framework for Efficient Photocatalytic CO_2 Conversion

Shengqian Yu[a#], Zicheng Wang[a#], Yihong Xie[b], Guangming Li[a]*, Feng-Ming Zhang[c]*, Yuxin Li[a]*

[a]Key Laboratory of Function Inorganic Material Chemistry (MOE), School of Chemistry and Material Science, Heilongjiang University.

[b]School of Modern Agriculture and Ecological Environment, Heilongjiang University, Harbin 150080, China.

[c]Heilongjiang Provincial Key Laboratory of CO_2 Resource Utilization and Energy Catalytic Materials, School of Material Science and Chemical Engineering, Harbin University of Science and Technology, Harbin 150080, China.

#These authors contributed equally to this work.

*Corresponding author: gmli@hlju.edu.cn (G.M. Li), zhangfm80@163.com (F.M. Zhang), liyuxin@hlju.edu.cn (Y.X. Li)

1.Experimental Methods

Material

Organic ligands 5-tetrazolylisophthalic acid (H_3TZI) were purchased from Jinan Henghua Technology Co., Ltd (China) and used after further purification. $PMo_{11}W$ (POM), *rht*-MOF-1 (MOF) and $PMo_{11}W$@*rht*-MOF-1 (POM@MOF) was synthesized according to a literature method.[1–3] $NiCl_2 \cdot 6H_2O$, $CuCl_2 \cdot 2H_2O$, $Na_2WO_4 \cdot 2H_2O$, $Na_2MoO_4 \cdot 2H_2O$, Na_2HPO_4 and anhydrous solvents were purchased from HWRK Chemicals (China) and used without further purification.

Synthesis

Synthesis of $Ni_xPMo_{11}W$ (Ni/POM, x=0.25, 0.50, 0.75, 1.00). The general prepared procedure for $Ni_{0.5}PMo_{11}W$ (Ni/POM) was as follows: Na_2HPO_4 (0.710 g, 5.00 mmol) and Na_2MoO_4 (13.308 g, 55.0 mmol) were dissolved in 30 mL of deionized water under constant stirring. The pH of the mixture was adjusted to 2.6 by adding concentrated sulfuric acid. Subsequently, a solution of Na_2WO_4 (1.649 g, 5.00 mmol) in 10 mL of deionized water was injected into the mixture. The pH of the solution was further adjusted to 3.5 using the same method. A solution of $NiCl_2 \cdot 6H_2O$ (0.594 g, 2.50 mmol) dissolved in 10 mL of deionized water was then added to the mixed solution, and the pH was adjusted again to 2.8 using the same method. The resultant solution was refluxed at 75 ℃ for 3 hours. After cooling to room temperature, the Ni/POM product was obtained via extraction with diethyl ether. Evaporate to crystallization, filter while hot, and dry to obtain a yellow-green powder. By varying the molar ratio of $NiCl_2 \cdot 6H_2O$ (1.25 mmol, 3.75 mmol, 5.00 mmol) in the feed, other Ni/POM ratios were prepared.

Synthesis of $Ni_xPMo_{11}W$@*rht*-MOF-1 (Ni/POM@MOF). $CuCl_2 \cdot 2H_2O$ (0.061 g, 0.360 mmol) and 5-tetrazolylisophthalic acid (H_3TZI) (0.022 g, 0.094 mmol) were dissolved in 2 mL of DMF. Subsequently, a solution of Ni/POM (0.105 g, 0.055 mmol) in 2 mL of deionized water was added to the above mixture under stirring. The resulting suspension was then transferred into a 25 mL Teflon-lined stainless steel autoclave and heated at 75 ℃ for 12 hours. After cooling to room temperature, the resulting cyan hexagonal crystal solid was washed with 20 mL of a mixture of

DMF and deionized water (1:1, v/v). Finally, the sample was dried under vacuum at 45 ℃ for 12 hours. By varying the type of Ni_x/POM used, other ratios of Ni_x/POM@MOF were prepared.

Characterization

The powder X-ray diffraction (XRD) patterns of the as-prepared samples were measured using a Bruker D8 Advance diffractometer with Cu Kα radiation. High-angle annular dark-field scanning transmission electron microscopy (HAADF-STEM) and energy-dispersive X-ray spectroscopy (EDS) elemental mappings were performed on a FEI Titan G2 60-300 STEM/TEM microscope at 300 kV. The UV-vis diffuse reflectance spectra (UV-vis DRS) and UV-vis absorption spectra of the samples were obtained using a Shimadzu UV2700 spectrophotometer, with $BaSO_4$ as the reference. Fourier-transform infrared (FT-IR) spectra of the samples were recorded on a PerkinElmer Spectrum 100 spectrometer, using KBr as the diluent. Thermogravimetric analysis (TGA) was conducted on a PerkinElmer STA 6000 simultaneous thermal analyzer under an air atmosphere with a heating rate of 10 ℃/min from room temperature to 800 ℃. Inductively coupled plasma atomic emission spectroscopy (ICP-AES) data were acquired using a Perkin-Elmer HK2000 spectrometer. X-ray photoelectron spectroscopy (XPS) spectra were recorded on an Escalab MK II spectrometer (VG Company, UK). All binding energies (BE) were calibrated to the BE of the C1s peak at 284.6 eV, providing BE values with an accuracy of ±0.1 eV. Time-resolved photoluminescence (TS-PL) spectra were measured using a single-photon counting spectrometer (Edinburgh Instruments, FLS 920) with a 1 μs pulse lamp as the excitation source. Electron paramagnetic resonance (EPR) measurements were performed to detect ·OH and $\cdot O_2^-$ radicals, which were trapped by 5,5-dimethyl-1-pyrroline N-oxide (DMPO), producing EPR signals of their adducts. For EPR analysis, the sample (5 mg) was dissolved in DMPO solution with H_2O/MeOH as the solvent to prepare the liquid mixture. After illumination, the mixture was characterized using a Bruker EMX Plus spectrometer at room temperature. CO_2 adsorption measurements were carried out using a Micromeritics 3Flex instrument (USA).

X-ray absorption fine structure (XAFS) spectroscopy

Ni K-edge XAFS analyses were performed using Si (111) crystal monochromators at the BL14W beamline of the Shanghai Synchrotron Radiation Facility (SSRF) (Shanghai, China). Prior to analysis, the samples were placed into aluminum sample holders and sealed with Kapton tape film. The XAFS spectra were recorded at room temperature using a 4-channel Silicon Drift Detector (SDD) (BNiker 5040). Ni K-edge extended X-ray absorption fine structure (EXAFS) spectra were collected in fluorescence mode. Negligible changes in the line-shape and peak position of Ni K-edge XANES spectra were observed between two scans taken for a specific sample. The XAFS spectra of standard samples were recorded in transmission mode. The spectra were processed and analyzed using the software package Athena, and EXAFS data fitting was performed with the Artemis program.[4]

Transient absorption spectroscopy (fs-TAS)

The fs-TAS measurements were performed on a Helios pump-probe system (Ultrafast Systems LLC) combined with an amplified femtosecond laser system (Coherent). Optical parametric amplifier (TOPAS-800-fs) provided a 320 nm pump pulse (~ 0.1 μJ/pulse), which was excited by a Ti: sapphire regenerative amplifier (Legend Elite-1K-HE; 800 nm), 35 fs, 7 mJ/pulse, 1 kHz and seeded with a mode-locked Ti: sapphire laser system (Micra 5) and an Nd: YLF laser (EvolutIon 30) pumped. Focusing the 800 nm beams (split from the regenerative amplifier with a tiny portion, 550nm). The pulse-to-pulse fluctuation of the WLC is corrected by a reference beam split from WLC. A motorized optical delay line was used to change the time delays (0–8 ns) between the pump and probe pulses. The instrument response function (IRF) was determined to be ~100 fs by a routine cross-correlation procedure. A mechanical chopper operated at a frequency of 500 Hz used to modulate the pump pulses such that the fs-TAS spectra with and without the pump pulses can be recorded alternately.

Electrochemical (EC) experiments

Electrochemical (EC) reduction measurements were conducted in a traditional three-electrode system. The prepared thin-film electrode, a platinum plate (99.9%), and an Ag/AgCl electrode were used as the working, counter, and reference electrodes, respectively. A 0.1 M solution of 1-butyl-3-methylimidazolium hexafluorophosphate in dichloromethane was used as the electrolyte. High-purity nitrogen gas (99.999%) was bubbled through the electrolyte before and during the experiments. An IVIUM V13806 electrochemical workstation was employed to evaluate the electrochemical performance of the series of catalysts. All experiments were performed at room temperature (approximately 25 °C).

In-situ electron paramagnetic resonance (EPR)

The in-situ EPR signal measurements were performed using a Bruker A300 spectrometer. The center field was set to 3500.00 G, the swept field width to 150.00 G, the sweep time to 30.00 s, the microwave power to 3.99 mW, the modulation amplitude to 1.000 G, and the conversion time to 40.0 ms at a frequency of 9.854854 GHz. Under a nitrogen atmosphere, a 500 W mercury lamp was used as the light source to irradiate the 5 mg sample. The EPR signals were measured at various time intervals.

In-situ X-ray photoelectron spectroscopy (XPS)

In the experiment for XPS testing under illumination, the silicon wafer was first cleaned using the Radio Corporation of America (RCA) method and cut into 1 cm × 1 cm pieces, which were then fixed onto the XPS sample holder. A 300 W xenon lamp was used as the light source, with the distance between the lamp and the sample set to 10 cm, the power set to 100 mW/cm², and the illumination time set to 30 minutes. The sample was illuminated in a nitrogen environment to ensure that the temperature did not exceed 50 °C. After illumination, the sample was immediately transferred to the XPS analysis chamber. XPS spectra were recorded using a VG ESCALAB apparatus with a Mg Kα X-ray source to determine the elemental chemical state and surface composition of the tested samples. The binding energies were calibrated with respect to the signal for adventitious carbon (binding energy = 284.6 eV). Additionally, a 370 nm laser was used as the light source to obtain the in-situ XPS spectra under illumination.

In-situ diffuse reflectance infrared spectra (DRIFTS)

A transmission in situ DRIFTS setup was used to investigate the effective CO_2 adsorption on the sample surface. The samples were loaded into the sample holder with a flat surface. A cover was fixed onto the sample holder to form a reaction space, which was then purged with argon gas. The initial DRIFTS data were collected as the background. Subsequently, visible light was introduced into the reaction space through an observation window, and CO_2 was introduced through a container filled with water, allowing the gas to carry water vapor into the reaction space. DRIFTS data were then collected over time, and the changes in the spectra were recorded.

Photocatalytic performance measurements

Photocatalytic CO_2 reduction: In the photocatalytic reduction of CO_2, 0.005 g of the powder sample and 0.030 g of tris(2,2'-bipyridyl)ruthenium ($[Ru(bpy)_3]^{2+}$) were dispersed in a mixture of acetonitrile (3 mL), water (1 mL), and triethanolamine (1 mL) in a cylindrical steel reactor with a volume of 120 mL. A 300 W Xe lamp was used as the light source. Highly pure CO_2 gas was introduced into the reactor to reach ambient pressure. The photocatalyst was equilibrated in the CO_2/H_2O system for 1 hour prior to irradiation. During irradiation, 0.5 mL of the gaseous mixture was withdrawn from the reaction cell at specific time intervals for subsequent concentration analysis. The concentrations of CO were determined using a gas chromatograph (GC-7980, Techcomp) equipped with a flame ionization detector (FID) and a CO_2 converter, while H_2 was analyzed using a thermal conductivity detector (TCD) with a molecular sieve (5 Å) and an Ar carrier gas.[5]

Recycle test: The recycling test was conducted following the same procedure. After each run, the used photocatalyst was separated, washed with a large amount of water, and then dried at 45 ℃ in a vacuum oven for the next cycle. Any loss during the recycling process was replenished with fresh photocatalyst.

Gas evolution rate study:

$$R = \frac{\rho \cdot V \cdot a \cdot 10^{-6}}{M \cdot m \cdot t}$$

In the equations, $\boldsymbol{R}$ (mol·g^{-1}·h^{-1}) represents the yield of the generated gas. $\boldsymbol{\rho}$ (g/L) represents the density of the generated gas. $\boldsymbol{V}$ (L) represents the volume of the reaction vessel. $\boldsymbol{a}$ (ppm) represents the gas phase integral data (ppm). $\boldsymbol{M}$ (g/mol) represents the molar mass of the generated gas. $\boldsymbol{m}$ (g) represents the mass of the catalyst. $\boldsymbol{t}$ (h) represents the reaction time.

Calculation for CO Selectivity:

We have calculated the selectivity based on the previous literature reports using the following equation[4]

$$Selectivity_{CO} = \frac{2 \cdot n_{CO}}{2 \cdot n_{CO} + 2 \cdot n_{H_2}} \times 100\%$$

Where we have accounted the number of electrons required to convert CO_2 to CO as well as the yield (μmol) of the products in the CO_2 photoreduction process. The product selectivity for CO_2 reduction to CO on an electronic basis ($2e^-$ for the formation of CO and $2e^-$ for H_2) has been calculated using the following equation, where n represented the yield (μmol) of the products in the CO_2 photoreduction after 4 h.

Statistical analysis: All data are presented as mean ± standard deviation (SD). The sample size for each statistical analysis was three. To test the significance of the observed differences between the study groups, analysis of variance (ANOVA) was applied, and a P-value of < 0.05 was considered statistically significant.

Theoretical Calculation Methodology

Our spin-polarized density functional theory (DFT) calculations[6,7] were performed using the Vienna Ab Initio Simulation Package (VASP) with plane-wave basis sets and the projector augmented-wave (PAW) method.[8,9] The exchange-correlation potential was described using the generalized gradient approximation (GGA) with the Perdew-Burke-Ernzerhof (PBE)

parametrization.[10] To account for van der Waals interactions, Grimme's DFT-D3 correction was employed.[11] The cluster model was placed in a cubic box with a lattice length of 25 Å to avoid interactions between adjacent images. The energy cutoff was set to 450 eV, and the Brillouin-zone integration was sampled at the Gamma point (1 × 1 × 1). Structural optimizations were carried out until the maximum force on each atom was less than 0.04 eV/Å, and the energy convergence criterion was set to 10^{-5} eV. The Gibbs free energies of the intermediates were calculated using the following expression:

$$\Delta G = \Delta E + \Delta \mathrm{E_{ZPE}} + \Delta H_{0\to T} - T\Delta S$$

where ΔE denotes the change in electronic energy obtained from DFT, $\Delta \mathrm{E_{ZPE}}$, $\Delta H_{0\to T}$ and ΔS are the changes of the zero-point energy, the enthalpy and entropy at standard conditions (T= 298 K and at potential vs NHE).

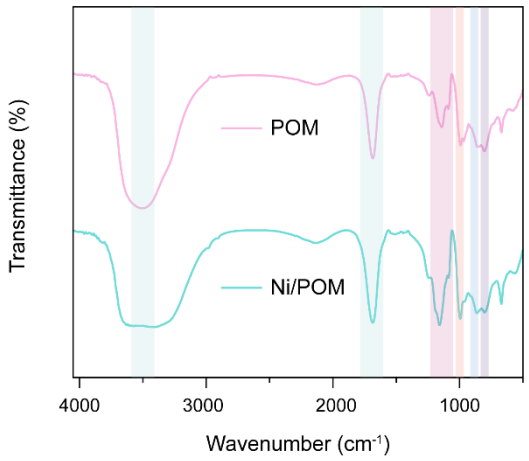

Supplementary Figure 1 | FT-IR spectra of the POM and Ni/POM.

The synthesis precursors of POM ($PMo_{11}W$) include PO_4^{3-}, WO_4^{2-}, and MoO_4^{2-}. The synthesized POM exhibits four characteristic peaks of the Keggin structure in the range of 700–1100 cm^{-1}. The characteristic peak at 1090 cm^{-1} is attributed to the stretching vibration of the P-O_a bond, the peak at 941 cm^{-1} to the stretching vibration of the M=O_d bond, the peak at 813 cm^{-1} to the stretching vibration of the M-O_b-M bridge bond, and the peak at 753 cm^{-1} to the stretching vibration of the M-O_c-M bridge bond. Additionally, the characteristic peaks at 3500 cm^{-1} and 1634 cm^{-1} are assigned to the O-H bond vibrations of water molecules. Notably, these characteristic peaks are also clearly visible in the Ni/POM after single-atom loading. Furthermore, due to the differences in the Mo and W contents in POM, the characteristic peaks may shift, but no such phenomenon was observed in Ni/POM. Therefore, it can be initially confirmed that the Ni loading did not induce any changes in the original POM structure and its components.

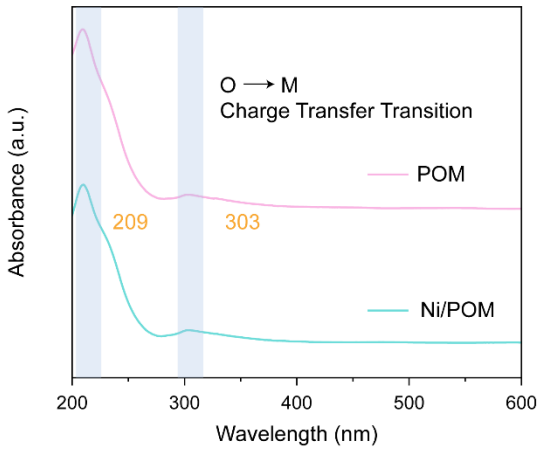

Supplementary Figure 2 | UV-Vis spectra of the POM and Ni/POM.

The UV-Vis spectral characteristic peaks of Keggin-POMs usually appear in the range of 200–350 nm, corresponding to the O to Metal (M) charge transfer transitions. In the synthesized POM spectrum, distinct characteristic peaks can be observed at 209 nm and 303 nm. These peaks indicate the O to M charge transfer transition in the Keggin structure. In the modified Ni/POM spectrum, these two characteristic peaks (209 nm and 303 nm) remain clearly visible, proving that the Keggin structure is preserved after Ni loading without significant changes. It can be inferred that the introduction of Ni does not disrupt the basic structure of POM, and the characteristics of the Keggin structure remain intact.

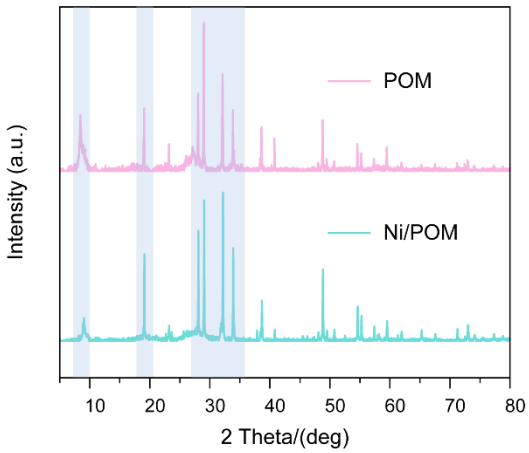

Supplementary Figure 3 | PXRD spectrum of POM and Ni/POM.

The PXRD characteristic peaks of Keggin-POMs are primarily concentrated in the ranges of 2θ = 8–10°, 17–20°, 26–30°, and 33–35°. First, it can be observed that in the unmodified POM sample, the diffraction peaks appear at 2θ = 8°, 19°, and 27–34°, indicating the perfect Keggin structure. Additionally, diffraction peaks in the range of 2θ = 45–55° are attributed to the presence of crystallized water. In the case of the single-atom modified Ni/POM sample, these structural characteristic peaks are clearly observed at their original positions, and no new diffraction peaks are observed. This confirms that the introduction of single-atom Ni has not led to any changes in the original structure of POM.

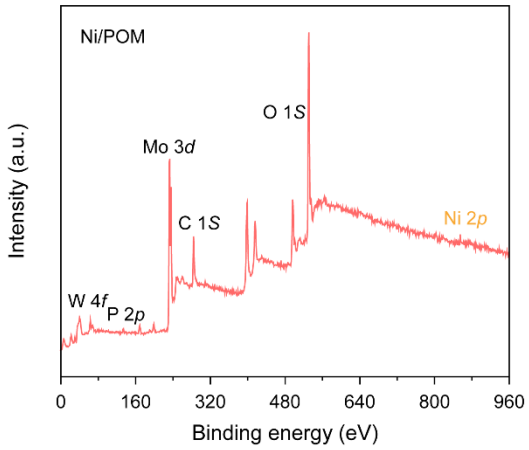

Supplementary Figure 4 | XPS spectra of Ni/POM.

The XPS spectrum of Ni/POM clearly shows the characteristic peaks of the main elements of POM, including W 4*f*, Mo 3*d*, P 2*p*, and O 1*s*, indicating that the original elements of POM are fully retained during the modification process. In addition, the characteristic peak of Ni 2*p* is also clearly visible, further confirming the successful incorporation of single-atom Ni. These results indicate that the loading of Ni has not damaged the intrinsic structure of POM while achieving the effective loading of Ni.

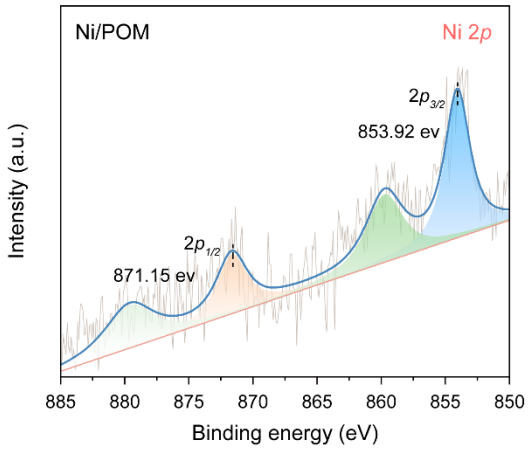

Supplementary Figure 5 | Ni 2*p* XPS spectra of Ni/POM.

In the XPS spectrum of Ni/POM, the characteristic peaks of Ni *2p* are clearly observed, with binding energies of 853.92 eV and 871.15 eV for $2p_{3/2}$ and $2p_{1/2}$, respectively. The existence of these characteristic peaks clearly confirms the successful incorporation of Ni.

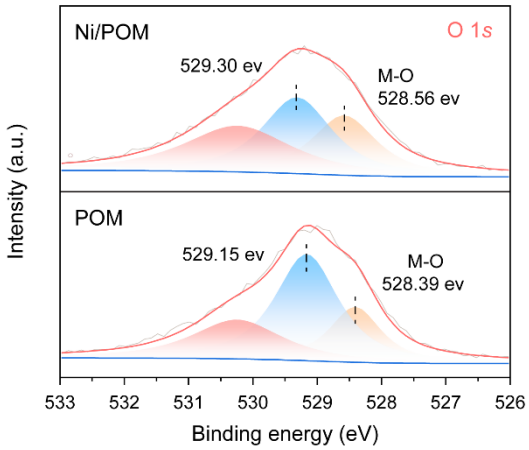

Supplementary Figure 6 | O 1*s* XPS spectra of Ni/POM.

The comparison of O 1*s* XPS spectra of Ni/POM and POM samples clearly shows the shift in binding energy. In the POM sample, the binding energies of O 1*s* are primarily located at 529.15 eV and 528.39 eV, corresponding to oxygen in metal oxides (M-O). In the Ni/POM sample, these binding energies shift positively to 529.30 eV and 528.56 eV, respectively. This shift in binding energy clearly demonstrates that the introduction of Ni forms chemical bonds with the oxygen atoms in POM, completing the Ni loading.

Table S1. ICP-AES of Ni/POM and Ni/POM@MOF.

Sample	P (wt.%)	Mo (wt.%)	W (wt.%)	Ni (wt.%)	Cu (wt.%)
Ni/POM	0.75	16.41	4.32	0.85	-
Ni/POM@MOF	0.27	2.30	0.75	0.48	19.96

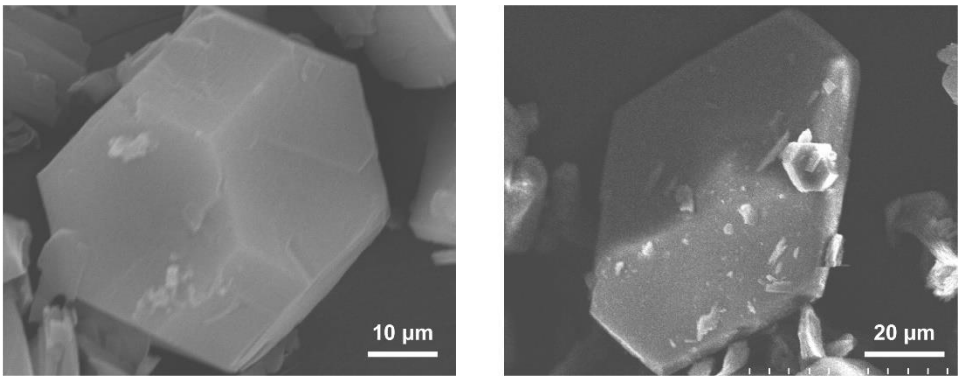

Supplementary Figure 7 | SEM structure of Ni/POM@MOF.

The Ni/POM@MOF sample exhibits a distinct polyhedral shape in the SEM images, with clear facets and edges, and the crystal surface is relatively smooth and regular, displaying a good geometric shape. This indicates that during the Ni loading and POM introduction process, the crystal structure of the MOF remains intact, still forming a stable and well-crystallized material. Furthermore, the polyhedral shape and clear edges of the material further demonstrate that the Ni loading has not significantly affected the coating of the MOF, thus preserving the intrinsic structural features of the MOF.

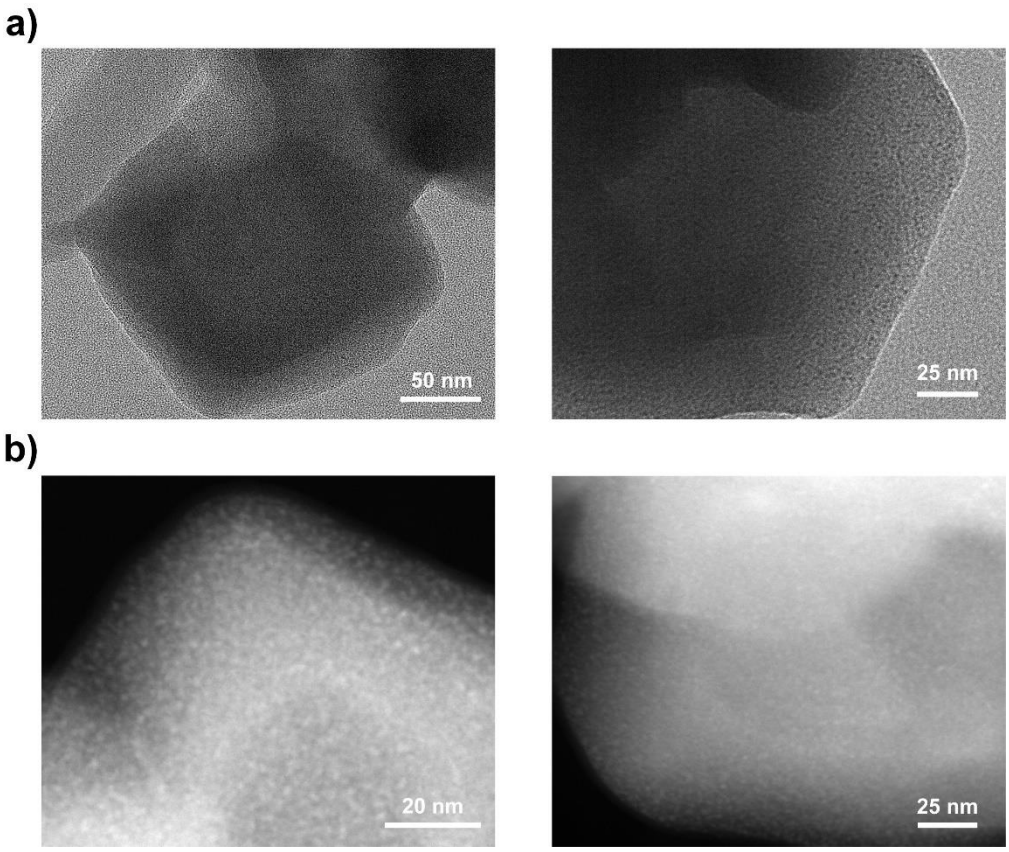

Supplementary Figure 8 | a) HR-TEM image and b) HAADF-STEM image of Ni/POM@MOF. The polyhedral morphology of Ni/POM@MOF can be clearly observed through HR-TEM and HAADF-STEM images. In the HR-TEM image, black dots are evenly distributed throughout the interior and on the surface of the MOF, while in the HAADF-STEM image, bright spots are clearly distributed within the MOF structure. These black and bright spots can be attributed to the successful encapsulation of Ni/POM. This result indicates that Ni/POM is uniformly distributed and effectively loaded within the MOF, and the introduction of Ni has not disrupted the encapsulation effect of the MOF.

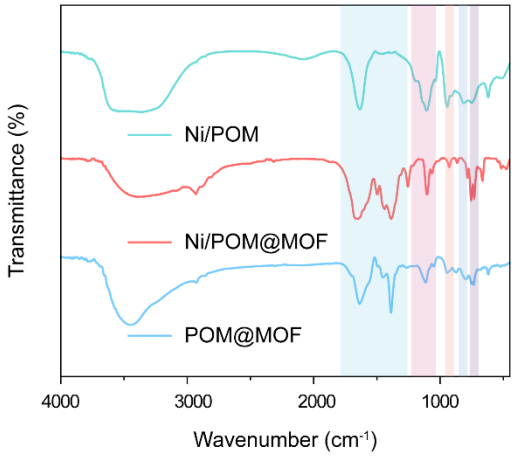

Supplementary Figure 9 | FT-IR spectra of Ni/POM, Ni/POM@MOF and POM@MOF.

The analysis of the infrared spectrum shows that the Ni/POM@MOF composite material exhibits characteristic peaks corresponding to its individual components. The characteristic peaks of the Keggin structure at 1090 cm^{-1}, 941 cm^{-1}, 813 cm^{-1}, and 753 cm^{-1}, which belong to Ni/POM, are clearly visible. In addition, the carboxyl vibration peaks in the range of 1655–1385 cm^{-1} in MOF are also clearly present in the composite material. The presence of these characteristic peaks preliminarily proves that MOF successfully encapsulated Ni/POM, forming the Ni/POM@MOF composite material. Furthermore, by comparing the structure of POM@MOF, it can be seen that the structures of the two composite materials are consistent. This also indicates that the introduction of Ni did not affect the encapsulation of Ni/POM within the MOF pores after loading. These results indicate that the synthesis of the Ni/POM@MOF composite material was successful and that its structural characteristics remain stable.

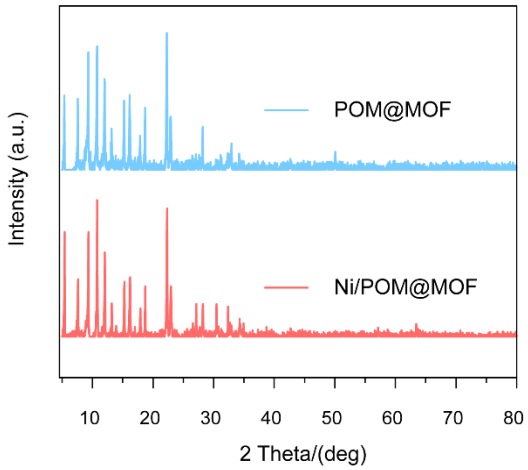

Supplementary Figure 10 | PXRD spectrum of POM@MOF and Ni/POM@MOF.

The PXRD patterns of POM@MOF and Ni/POM@MOF exhibit almost identical diffraction peak positions and intensities, suggesting that both materials have a similar crystal structure. After introducing Ni, the PXRD pattern of Ni/POM@MOF does not exhibit any significant shifts or new diffraction peaks, suggesting that the introduction of Ni did not damage the intrinsic structure of the material. The original features of the material are fully preserved, further proving that the successful loading of Ni was achieved without altering the original structure of the material.

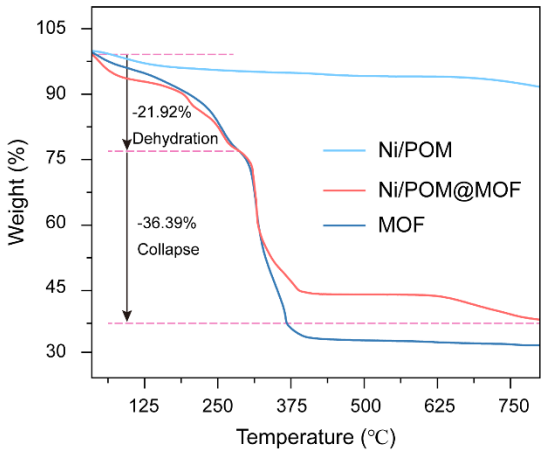

Supplementary Figure 11 | Thermogravimetric analysis (TGA) of Ni/POM, Ni/POM@MOF, and MOF. The thermogravimetric analysis (TGA) curve shows that Ni/POM exhibits stable mass changes over the entire temperature range, indicating its good stability at high temperatures. In contrast, Ni/POM@MOF and MOF undergo multiple mass loss processes. At approximately 125 °C, both MOF and Ni/POM@MOF show significant mass loss of about 21.92%, attributed to the dehydration process, which involves the loss of coordinated water and crystallization water in the sample. Between 250 °C and 375 °C, a second significant mass loss occurs. For Ni/POM@MOF, the mass loss is about 36.39%, which is related to the collapse of the structure and the thermal decomposition of organic components in the sample. In contrast, the mass loss of MOF is greater, indicating that the introduction of Ni/POM enhances the thermal stability of MOF. The TGA spectrum analysis shows that the introduction of Ni/POM not only improves the overall thermal stability of MOF but also reduces its mass loss at high temperatures. This result indicates that Ni/POM@MOF has better structural stability and thermal decomposition resistance under high-temperature conditions.

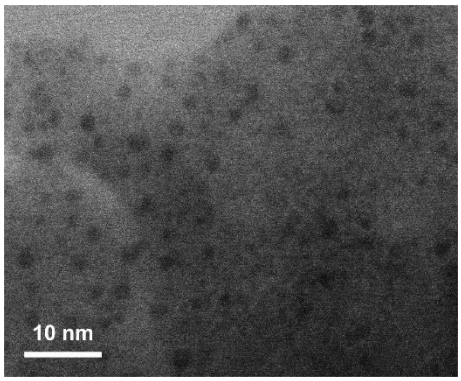

Supplementary Figure 12 | AC-TEM image of Ni/POM@MOF.

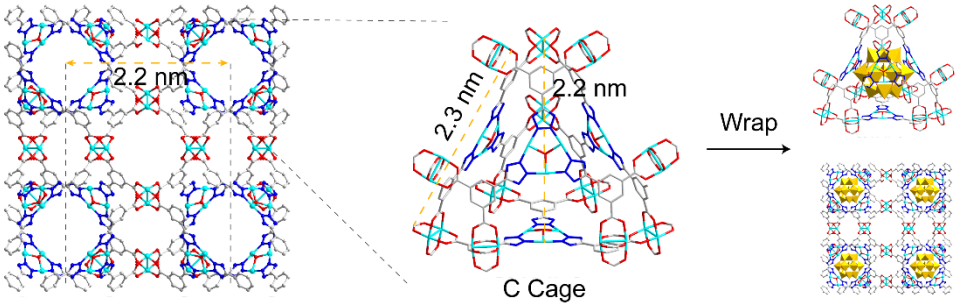

Supplementary Figure 13 | Structural illustration of the MOF. The framework consists of well-defined cavities with a diameter of 2.2 nm, forming a C cage with a triangular arrangement (2.3 nm). The right panel shows the wrapping process and integration of the structural units into the overall MOF framework.

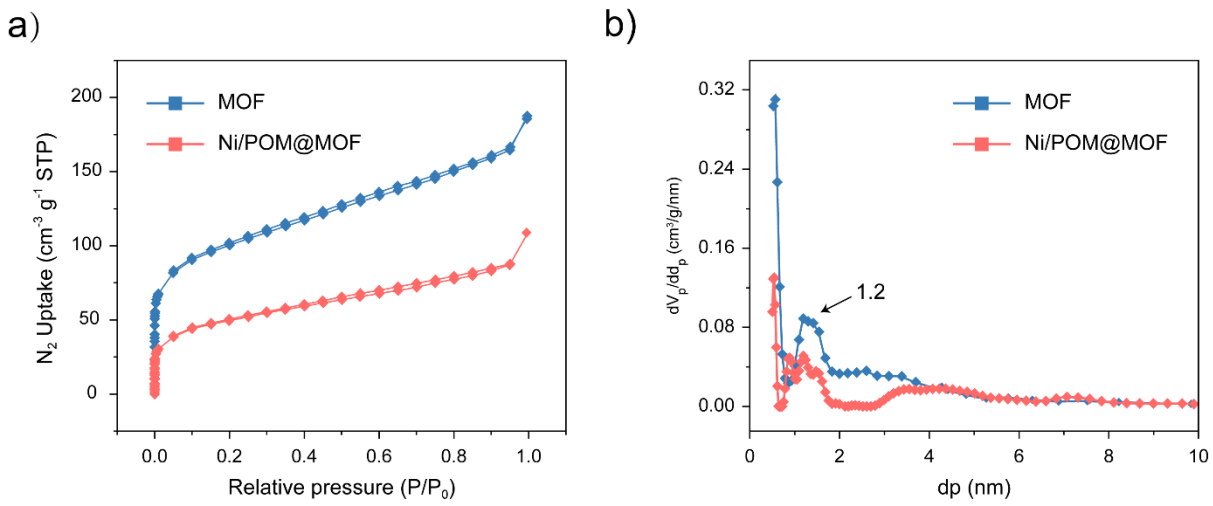

Supplementary Figure 14 | a) Comparison of N_2 adsorption isotherms and b) graph of the pore-size distribution of MOF and Ni/POM@MOF. Both exhibit typical Type IV isotherms, with large specific surface areas and pore volumes, and the pore size is mainly concentrated around 1.2 nm, with a certain number of mesopores. Ni/POM@MOF composite material has lower nitrogen adsorption capacity and pore volume compared to pure MOF, indicating that the introduction of Ni/POM occupies part of the MOF channels, resulting in a decrease in specific surface area and pore volume. The pore size distribution diagram shows that the pore size of Ni/POM@MOF is mainly concentrated around 1.2 nm, but the pore volume is significantly reduced, especially in the mesoporous region, further supporting the successful encapsulation of Ni/POM in the MOF channels.

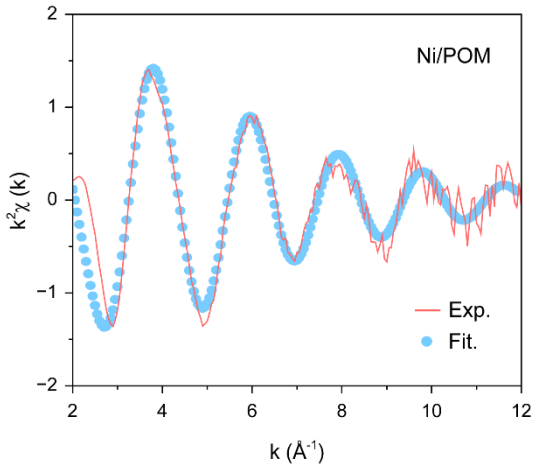

Supplementary Figure 15 | EXAFS k space fitting and the experimental curves of Ni/POM.

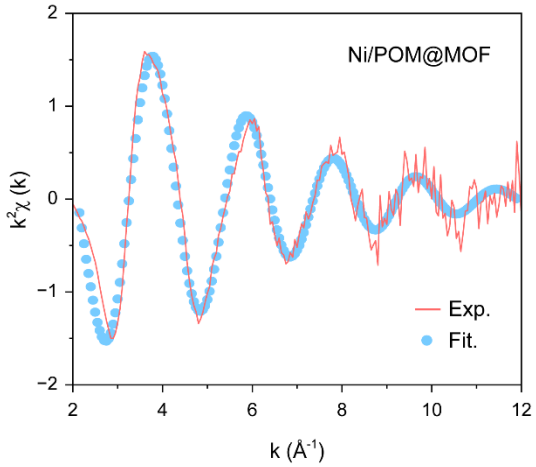

Supplementary Figure 16 | EXAFS k space fitting and the experimental curves of Ni/POM@MOF.

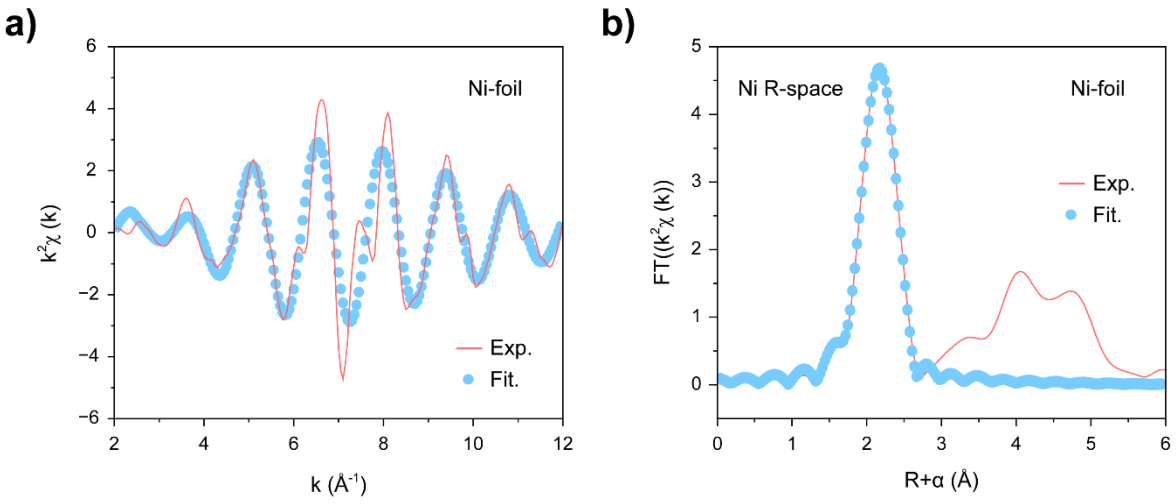

Supplementary Figure 17 | a) EXAFS k space fitting and the experimental curves of Ni-foil. b) FT-EXAFS fitting curves of Ni-foil.

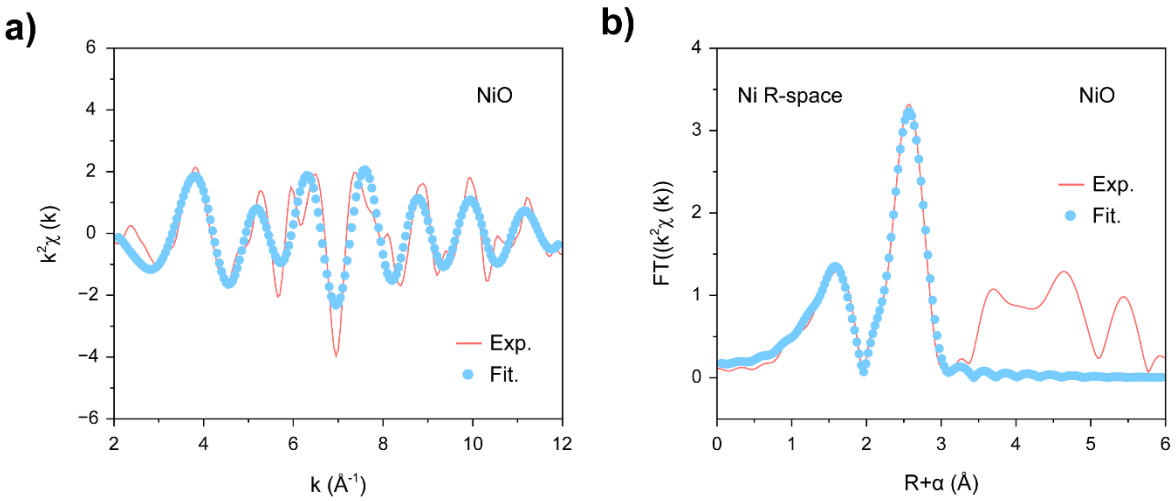

Supplementary Figure 18 | a) EXAFS k space fitting and the experimental curves of NiO. b) FT-EXAFS fitting curves of NiO.

Supplementary Figures 28–31 present the EXAFS experimental data and fitting results for Ni/POM, Ni/POM@MOF, Ni-foil, and NiO samples, including the EXAFS data in k-space and the R-space data obtained from Fourier transform. By comparing the experimental data and fitting results, it can be observed that the experimental data and fitting results match well in both spaces, indicating that the fitting model used can accurately describe the local structural features of these

samples. Specifically, the k-space data and R-space data of the Ni/POM sample show the presence of Ni-O bonds, and the good agreement between the fitting results and experimental data further validates the accuracy of these interactions. For the Ni/POM@MOF sample, the k-space and R-space data show the presence of Ni-O bonds, and the fitting results suggest the structural stability and uniform distribution of the composite material. The k-space and R-space data for the Ni-foil and NiO samples mainly show Ni-Ni and NiO bonds, and the good agreement between the fitting results and experimental data indicates that the arrangement of Ni atoms in the Ni samples conforms to the crystal structure of the Ni samples. These EXAFS data and fitting results provide detailed local structural information about the Ni/POM, Ni/POM@MOF, Ni-foil, and NiO samples, revealing the local environment and interactions of Ni atoms in the samples.

Table S2. EXAFS fitting parameters Ni/POM, Ni/POM@MOF, Ni-foil and NiO.

Sample	Path	d^b/Å	*N*	R/Å	σ^2/Å^2	R-factor	K space	R space
Ni/POM@MOF	Ni-O	2.11	6.0(6)	2.05(1)	0.007(1)	0.006	$3.0 \leq k \leq 10.0$ Å^{-1}	$1.0 \leq R \leq 2.5$ Å
Ni/POM	Ni-O	2.11	5.6(5)	2.03(1)	0.005(1)	0.007	$3.0 \leq k \leq 12.5$Å^{-1}	$1.0 \leq R \leq 2.5$Å
Ni-foil	Ni-Ni	2.48	12.00	2.48(1)	0.006(1)	0.001	$3.0 \leq k \leq 11.8$Å^{-1}	$1.0 \leq R \leq 2.69$ Å
NiO	Ni-O	2.11	6.0	2.08(1)	0.008(1)	0.008	$3.0 \leq k \leq 13.6$Å^{-1}	$1.0 \leq R \leq 3.2$Å
	Ni-Ni	2.98	12.0	2.95(1)	0.006(1)	0.009		

S_0^2 was fixed as 1.0. ΔE_0 was refined as a global fit parameter, returning a value of (6 ± 1) eV. The number of variable parameters is 4. The distances for Ni-O and are from the crystal structure of NiO. These coordination numbers were constrained as N(Ni-Ni) = 1 based on the crystal structure.

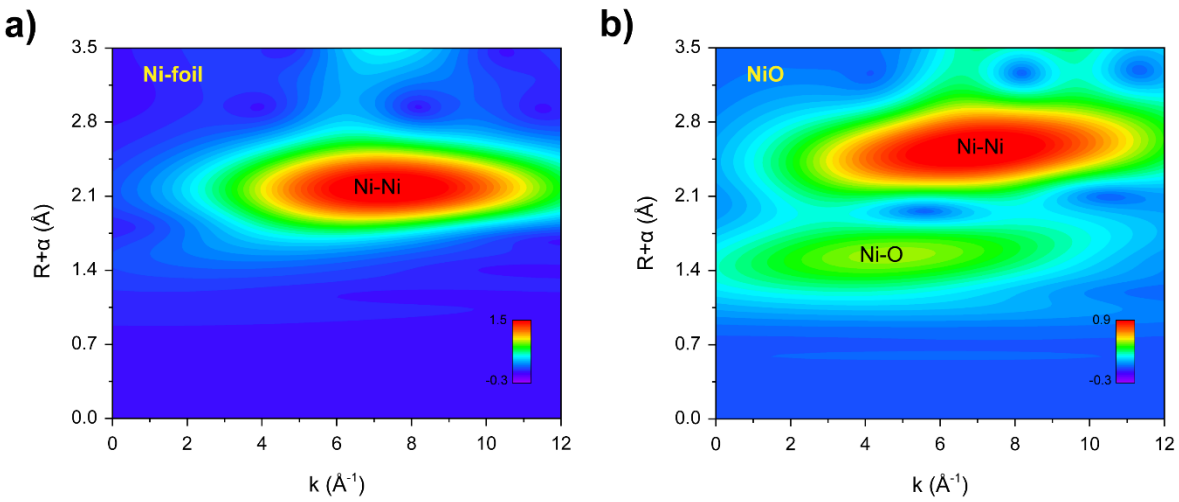

Supplementary Figure 19 | WT-EXAFS of a) Ni-foil and b) NiO.

Wavelet Transform (WT) is a signal processing technique that analyzes the local characteristics of a signal by decomposing it into components at different scales and frequencies.[14,15] Wavelet Transform differs from Fourier Transform (FT) in that it not only provides frequency information but also retains the local information of the signal in time or space. This gives the Wavelet Transform a unique advantage in processing non-stationary signals and performing multi-scale analysis. a) Ni-foil characteristic peak: The main characteristic peak in the figure appears at approximately 2.17 Å, corresponding to the Ni-Ni bond. This indicates that the Ni-foil sample mainly contains Ni-Ni interactions, reflecting the crystal structure of metallic Ni. b) NiO characteristic peaks: Two main characteristic peaks appear in the figure, at approximately 1.53 Å and 2.53 Å. The peak at 1.53 Å corresponds to the Ni-O bond, and the peak at 2.53 Å corresponds to the Ni-Ni bond.

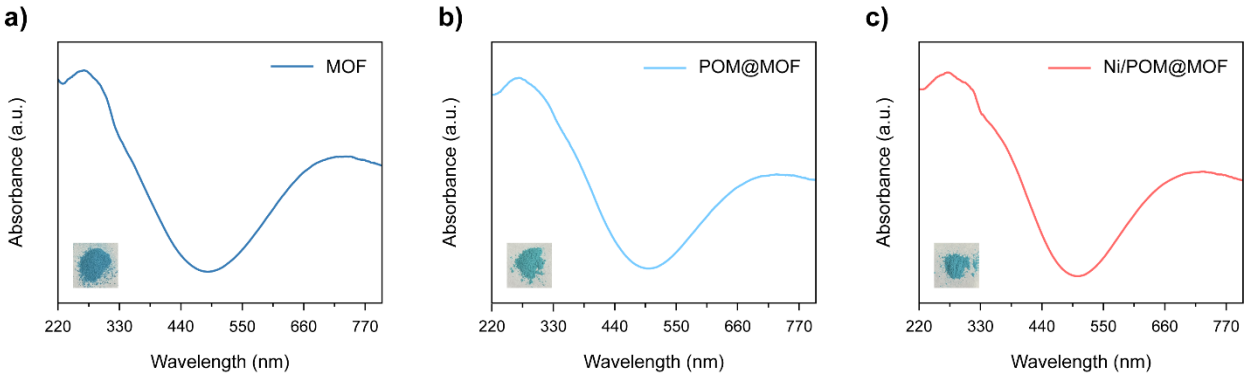

Supplementary Figure 20 | Solid-state UV/vis absorption spectra of a) MOF, b) POM@MOF and c) Ni/POM@MOF. As shown in Figure (a–c), the UV/Vis-NIR diffuse reflectance spectrum (DRS) of the material indicates that pure MOF exhibits significant absorption characteristics in the range of 250–400 nm and 600–700 nm, demonstrating its strong light capture ability in the ultraviolet and visible light regions. This indicates that in the composite material, MOF is the main light-absorbing unit. Furthermore, the change in the absorption spectrum is minimal, indicating that the intrinsic structure of MOF has not undergone significant alteration in the composite material.

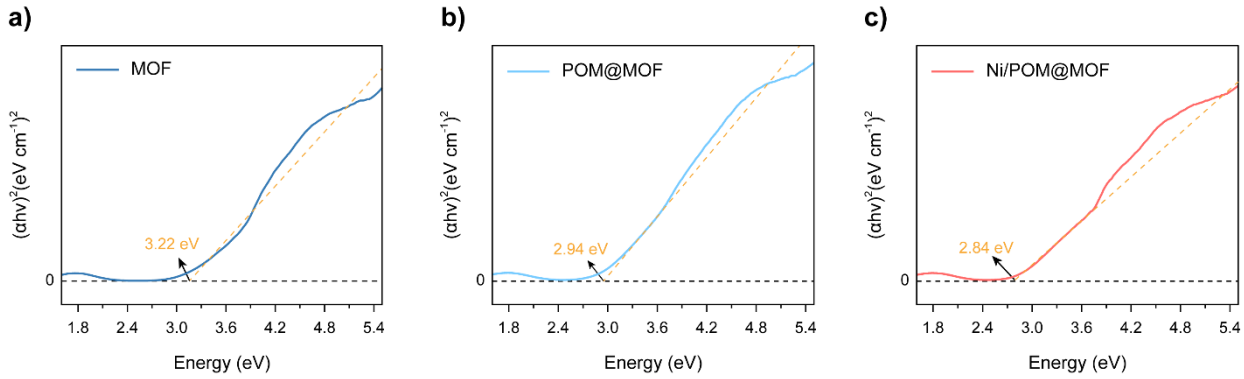

Supplementary Figure 21 | Tauc Relation Plot of a) MOF b) POM@MOF and c) Ni/POM@MOF by UV-Vis absorption spectra.

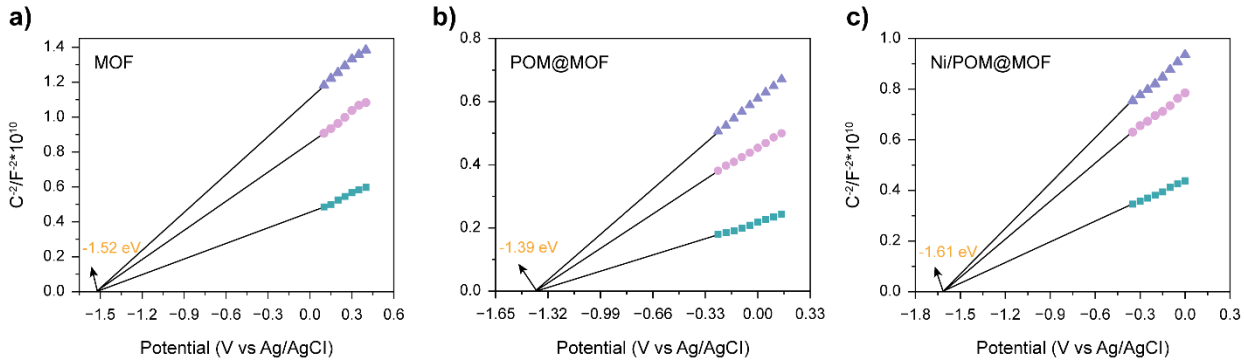

Supplementary Figure 22 | Mott-Schottky plot for a) MOF b) POM@MOF and c) Ni/POM@MOF.

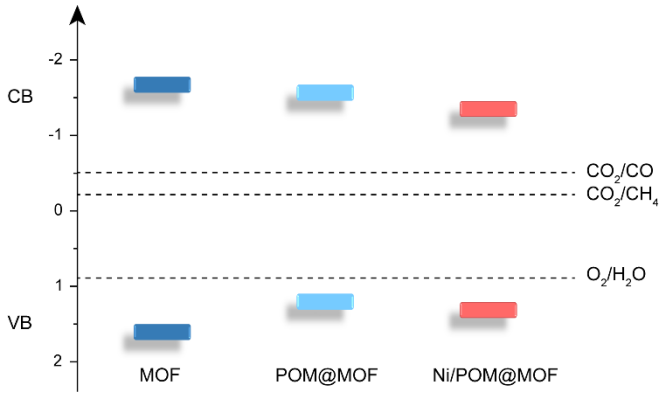

Supplementary Figure 23 | Band alignment of MOF, POM@MOF and Ni/POM@MOF.

The valence band (VB) and conduction band (CB) of each material were calculated based on the Mott-Schottky plot, and a comparative analysis was performed using a schematic diagram. The results are as follows:

MOF: CB = -1.52 eV, VB = 1.70 eV, EG = 3.22 eV

POM@MOF: CB = -1.61 eV, VB = 1.33 eV, EG = 2.94 eV

Ni/POM@MOF: CB = -1.39 eV, VB = 1.45 eV, EG = 2.84 eV

As shown in the figure, the conduction band (CB) positions of all three materials are lower than the reduction potentials for CO_2 reduction to CO (-0.52 eV) and CH_4 (-0.24 eV), indicating that they all possess thermodynamic driving forces for reducing CO_2 to CO or CH_4.

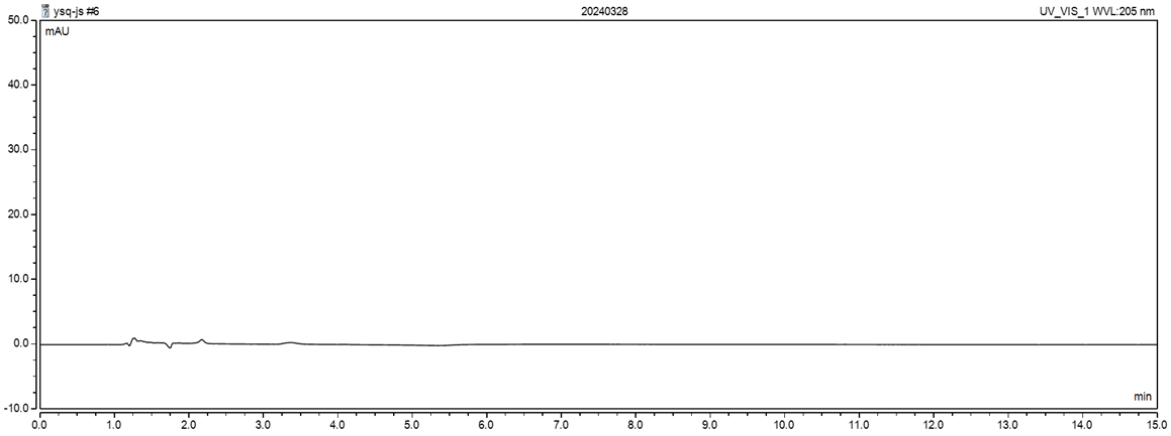

Supplementary Figure 24 | Liquid chromatography (LC) retention time of photoreduced CO_2 liquid products. Liquid-phase chromatography was employed to detect potential liquid-phase products at a wavelength of 205 nm. The chromatogram shows that no obvious product peaks appeared throughout the detection range. This suggests that no products were detected in the liquid phase, indicating that no liquid-phase products were formed under these conditions.

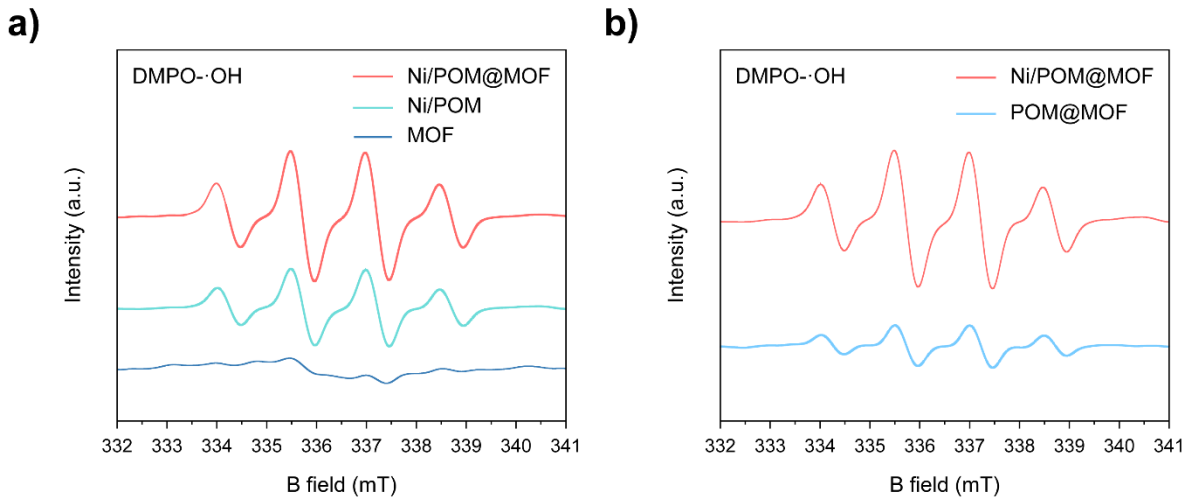

Supplementary Figure 25 | Hydroxyl radical signaling EPR spectra of a) Ni/POM@MOF, Ni/POM and MOF b) Ni/POM@MOF and POM@MOF. In the photocatalytic process, the photocatalyst absorbs photons, causing electrons to transition from the valence band to the conduction band, generating electron-hole pairs (e^-/h^+).[12] These electrons and holes can participate in various reactions, one of which is the generation of hydroxyl radicals. Holes (h^+) can oxidize water or hydroxide ions (OH^-) to generate hydroxyl radicals (·OH):

$$h^+ + H_2O \rightarrow \cdot OH + H^+$$

$$h^+ + OH^- \rightarrow \cdot OH$$

When the photocatalyst has an efficient electron-hole separation ability, more electrons and holes can be separated, reducing recombination. This allows more holes to participate in oxidation reactions, generating more hydroxyl radicals. The generation of hydroxyl radicals can be detected through EPR spectroscopy. Strong EPR signals indicate that a large amount of hydroxyl radicals is generated in the sample, reflecting efficient electron-hole separation. Ni/POM@MOF: If this composite material shows the strongest EPR signal, it indicates the most efficient electron-hole separation and the highest generation of hydroxyl radicals. In conclusion, EPR spectroscopy can effectively evaluate the electron-hole separation efficiency of different photocatalysts. Ni/POM@MOF composite shows the strongest EPR signal, indicating that it generates the most hydroxyl radicals during photocatalytic reactions, demonstrating the best electron-hole separation efficiency.

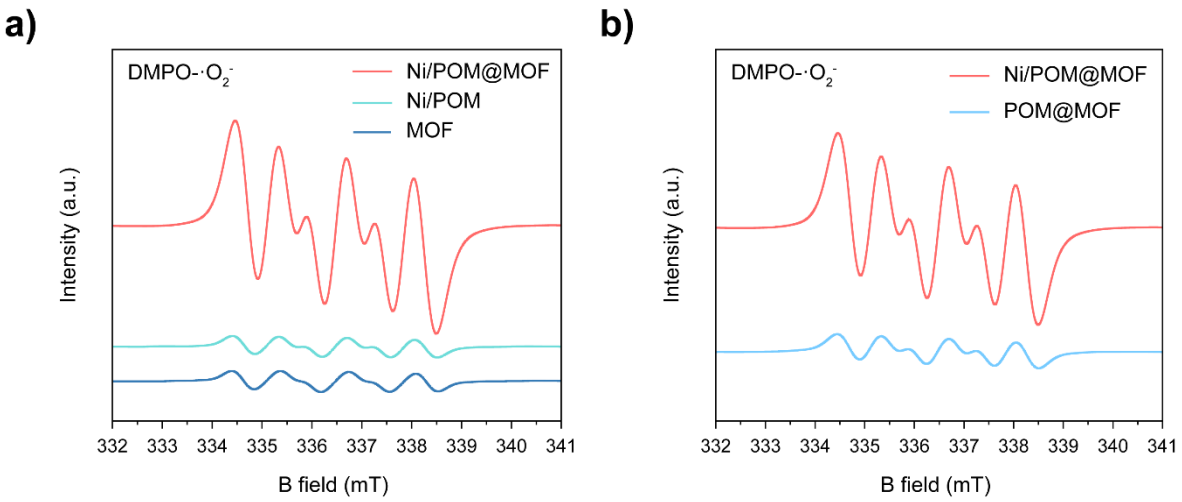

Supplementary Figure 26 | Superoxide radical signaling EPR spectra of a) Ni/POM@MOF, Ni/POM and MOF b) Ni/POM@MOF and MOF. The photocatalyst absorbs photons, causing electrons to transition from the valence band to the conduction band, forming electron-hole pairs.[13] The separated electrons can react with oxygen molecules adsorbed on the surface of the photocatalyst to generate superoxide radicals ($\cdot O_2^-$):

$$O_2 + e^- \rightarrow \cdot O_2^-$$

When the photocatalyst has an efficient electron-hole separation ability, more electrons and holes can be separated, reducing recombination. This allows more electrons to participate in the reaction to generate superoxide radicals. EPR spectroscopy shows that the EPR signal of Ni/POM@MOF is the strongest, indicating the highest generation of superoxide radicals, with the highest photocatalytic activity and electron-hole separation efficiency. Strong EPR signals mean that the material generates more superoxide radicals during the photocatalytic process, reflecting its higher photocatalytic performance and electron-hole separation efficiency. Ni/POM@MOF, due to its significantly enhanced electron-hole separation ability, exhibits the strongest EPR signal, indicating that it generates the largest amount of superoxide radicals during photocatalytic reactions. This demonstrates its excellent photocatalytic performance.

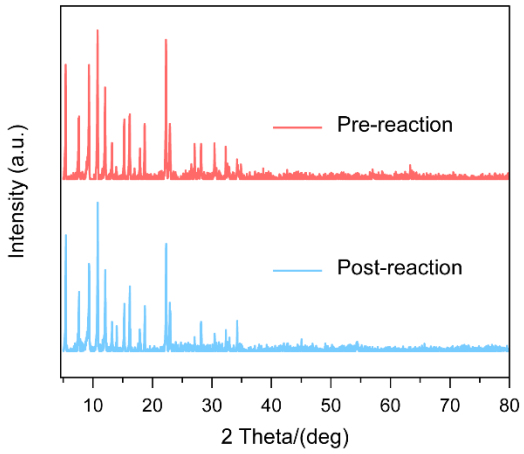

Supplementary Figure 27 | PXRD spectra of Ni/POM@MOF pre- and post- the catalytic reaction. In the XRD pattern, the crystal plane diffraction peaks in the 2θ range of 5–25° are still clearly visible, and the overall stability of the sample's crystal structure is well maintained. From the pattern, it can be seen that the diffraction peak intensity before the catalysis (Pre-reaction) is higher, while after the catalysis (Post-reaction), the peak intensity is weakened, but the position and shape of the peaks remain largely unchanged. These results suggest that the sample can still maintain its crystallinity during the catalysis process, and no significant structural collapse occurs. Although the diffraction peak intensity slightly decreases, this is likely due to minor changes on the surface or in some crystals during the catalysis process, rather than the destruction of the overall crystal structure. Overall, the XRD spectrum before and after catalysis demonstrates that the crystalline structure of the sample maintains good stability, retaining its characteristic crystallinity and structural features under catalytic conditions.

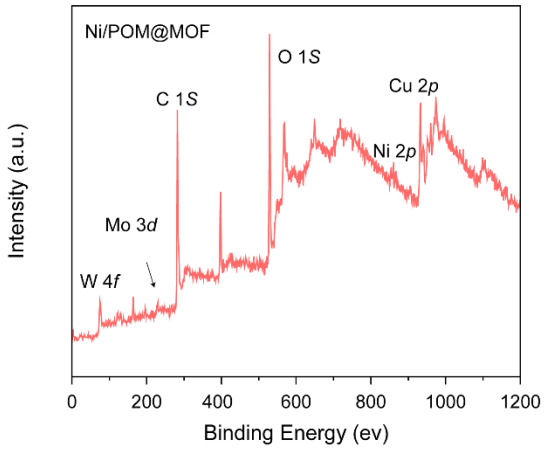

Supplementary Figure 28 | XPS spectra of Ni/POM@MOF post- the catalytic reaction.

In the XPS spectra of Ni/POM@MOF after the photocatalytic reaction, the characteristic peaks of elements like C 1*s*, O 1*s*, Ni 2*p*, Cu 2*p*, Mo 3*d*, and W 4*f* are clearly observed, suggesting that the catalyst's key elements remain intact after the reaction. This result proves that Ni/POM@MOF possesses excellent structural and chemical stability during the photocatalytic CO_2 reduction reaction. Furthermore, the presence of critical active elements (such as Ni and Mo) further suggests that the catalyst maintains the integrity of its intrinsic active sites after the reaction.

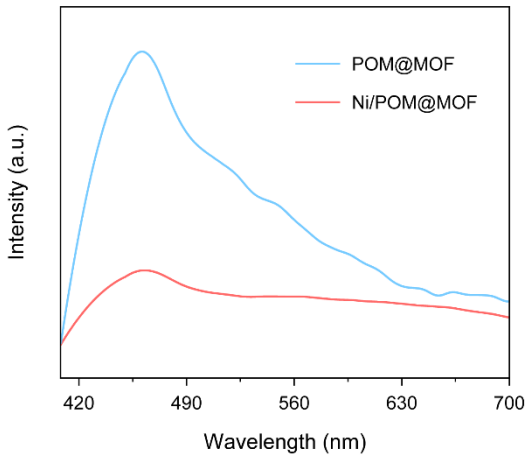

Supplementary Figure 29 | Photoluminescence spectra of POM@MOF and Ni/POM@MOF. The POM@MOF sample exhibits a higher photoluminescence (PL) intensity at 450 nm, indicating a higher recombination efficiency of the electron-hole pairs, meaning that the electrons and holes easily recombine and emit light. In contrast, the PL intensity of the Ni/POM@MOF composite material is significantly lower than that of POM@MOF, maintaining a lower intensity across the entire wavelength range. This is due to the introduction of Ni-SAEB, which increases the separation efficiency of the electron-hole pairs, indicating that the electrons and holes are more easily separated in the composite material, reducing the probability of recombination and light emission. This increase in electron-hole separation efficiency means that the utilization efficiency of photogenerated charge carriers is enhanced, which in turn improves the photocatalytic performance of the material. The decrease in PL intensity reflects an increase in non-radiative recombination pathways in the composite material, which helps more photogenerated electrons and holes participate in the photocatalytic reaction, enhancing photocatalytic activity. In conclusion, the Ni/POM@MOF composite material, by introducing Ni-SAEB, significantly enhances the electron-hole separation efficiency, reduces the photoluminescence intensity, and shows a higher photogenerated carrier utilization efficiency and superior photocatalytic performance in photocatalytic applications.

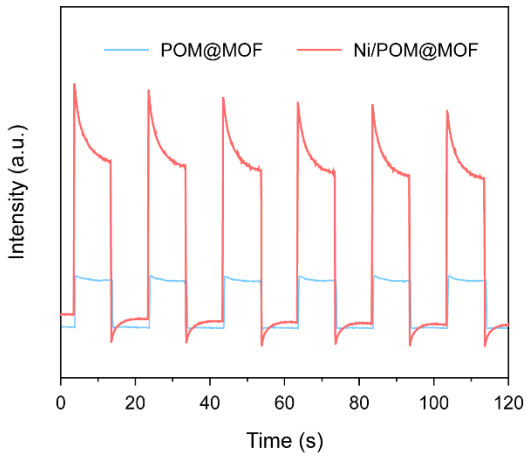

Supplementary Figure 30 | Transient photocurrent responses of POM@MOF and Ni/POM @MOF. Photoelectric current response testing is an important method for evaluating the electron-hole separation efficiency of photocatalysts. The photocurrent intensity of Ni/POM@MOF is significantly higher than that of POM@MOF, indicating that the introduction of Ni-SAEB effectively enhances the separation efficiency of photogenerated electron-hole pairs in the material. Higher photocurrent intensity means that under light irradiation, the material can generate more photogenerated electrons, and these electrons can efficiently separate and migrate, reducing recombination. The introduction of Ni-SAEB promotes electron transfer between POM and MOF, enhancing the electron transfer efficiency, thereby significantly improving the photocurrent response. This result fully demonstrates that the introduction of Ni-SAEB optimizes its electron transfer performance, providing key support for enhancing catalytic activity.

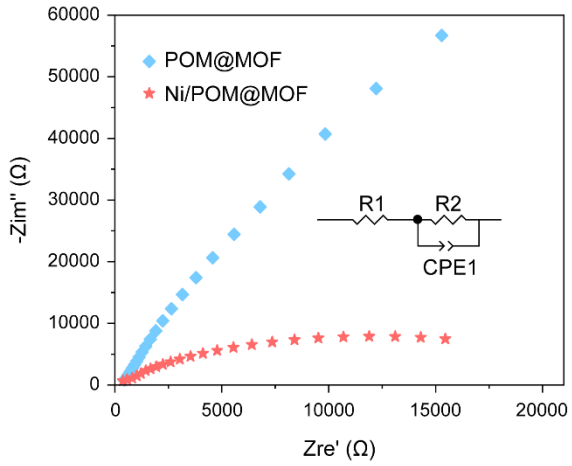

Supplementary Figure 31 | Electrochemical impedance spectroscopy (EIS) measurements of POM@MOF and Ni/POM@MOF. The charge transfer performance of POM@MOF and Ni/POM@MOF was characterized using electrochemical impedance spectroscopy (EIS).[16] In the Nyquist plot of Ni/POM@MOF, the semicircle diameter is significantly smaller than that of POM@MOF, indicating that the introduction of Ni significantly reduces the interfacial charge transfer resistance (R2). This reduction in impedance indicates that the introduction of Ni-SAEB enhances the electronic coupling between POM and MOF, facilitating efficient electron transfer. Moreover, Ni-SAEB optimizes the charge migration pathways of the material, significantly improving electron transport efficiency. This result further proves that the introduction of Ni-SAEB not only preserves the intrinsic structure of the material but also significantly enhances its charge transfer ability.

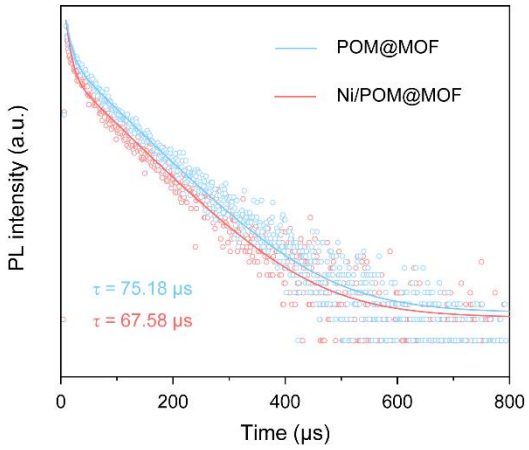

Supplementary Figure 32 | Time-resolved photoluminescence spectra of POM@MOF and Ni/POM @MOF.

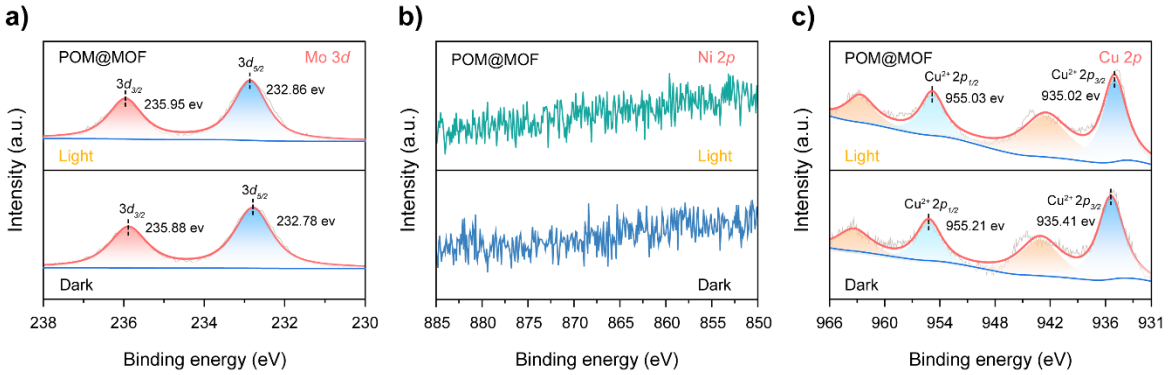

Supplementary Figure 33 | In situ XPS spectra of a) Mo 3*d* b) Ni 2*p* and c) Cu 2*p* signals in POM@MOF in after illumination.

The electronic transfer behavior of POM@MOF under light and dark conditions was analyzed using in situ XPS. In the Mo 3*d* spectrum (Figure a), under light conditions, the binding energy of Mo 3*d* shifts to a higher binding energy (235.88 eV → 235.95 eV), indicating that the Mo atoms in POM transferred electrons to the Cu sites in MOF. In the Cu 2p spectrum, the binding energy of Cu 2p shifts to a lower binding energy (935.41 eV → 935.02 eV), further confirming the electron transfer from POM to the Cu sites. However, no Ni 2*p* signal was detected in POM@MOF, indicating the absence of Ni-SAEB in the system. In this case, electron transfer solely relies on electrostatic interactions, and no effective electron cascade transfer channel is formed. Moreover, no valence change behavior was observed in the Cu 2*p* signal (Cu remains +2), indicating that without Ni-SAEB, the electron transfer efficiency is significantly reduced, and effective electron transfer cannot be achieved. Therefore, although POM@MOF shows some electron transfer pathways, its efficiency is much lower than that of Ni/POM@MOF containing Ni-SAEB. This result clearly demonstrates that the introduction of Ni-SAEB plays a key role in promoting electron transfer from POM to MOF and enhancing electron transfer efficiency, thus significantly improving the photocatalytic performance.

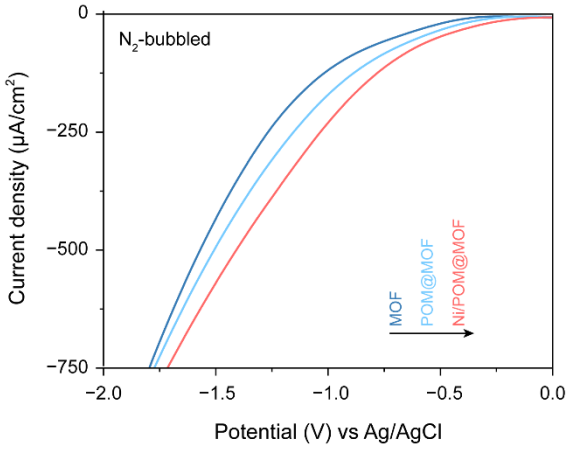

Supplementary Figure 34 | Electrochemical reduction curves of MOF, POM@MOF and Ni/POM@MOF in N_2-bubbled systems. From the comparison of electrochemical reduction performance, it can be seen that the current density of MOF is the lowest, indicating its poor electron transfer capacity and reduction performance. The current density of POM@MOF is significantly higher, indicating that the introduction of POM enhances electron transfer capacity, and POM, as an electron acceptor and transfer bridge, effectively improves the performance of MOF. Ni/POM@MOF has the highest current density, significantly higher than MOF and POM@MOF. This significant improvement is attributed to the introduction of Ni-SAEB, which acts as an efficient electron bridge, facilitating electron transfer between POM and MOF. These results clearly indicate that the presence of Ni-SAEB is the key factor in improving electron transfer efficiency and electrochemical performance.

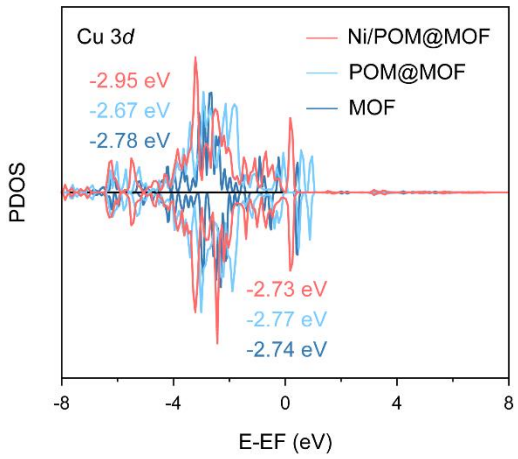

Supplementary Figure 35 | Cu 3*d* PDOS of Ni/POM@MOF, POM@MOF and MOF.

There are significant differences in the Cu 3*d* band center positions for Ni/POM@MOF, POM@MOF, and MOF. In MOF and POM@MOF, the Cu 3*d* band centers are located at -2.78 eV and -2.77 eV, respectively, indicating that the introduction of POM has little impact on the electronic structure of Cu. However, in Ni/POM@MOF, the Cu 3*d* band center shifts significantly to -2.73 eV. This change indicates that the introduction of Ni, through its synergistic effect with POM and MOF, significantly regulates the electronic structure of Cu, enhancing its adsorption activity towards CO_2 molecules. Additionally, the connecting role of Ni enhances the electronic coupling between POM and MOF, bringing the Cu *d*-band center closer to the Fermi level. This shift not only increases the affinity of Cu for CO_2 molecules but also promotes its activation ability towards CO_2, providing more efficient active sites for subsequent catalytic reactions. In summary, the introduction of Ni-SAEB regulates the electronic structure of Cu, significantly enhancing the CO_2 adsorption and activation ability of Ni/POM@MOF, providing theoretical support for its excellent catalytic performance.

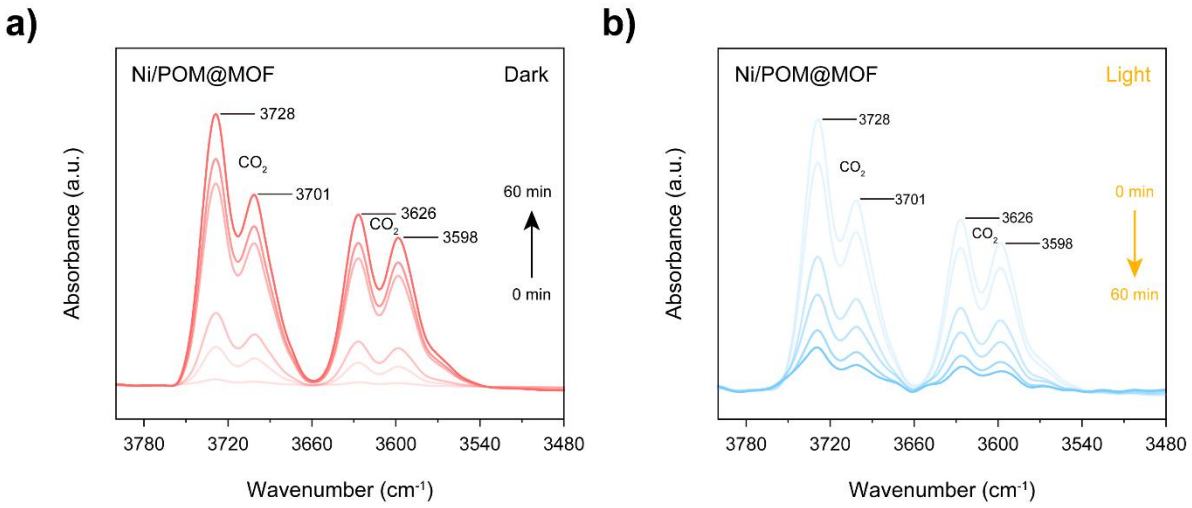

Supplementary Figure 36 | In situ DRIFT spectra for Ni/POM@MOF a) in dark and b) in light.

References

(1) Liu, S. W.; Gao, M.; Zhang, R. L.; Zhao, J. S. Template Method for a Hybrid Catalyst Material POM@MOF-199 Anchored on MCM-41: Highly Oxidative Desulfurization of DBT under Molecular Oxygen. *Fuel* **2016**, *184*, 18–27.

(2) Xin, Y.; Bai, Y.; Liu, J.; Ma, L.; Li, G. Effective Heterogeneous Oxidative Desulfurization Catalyzed by $H_3PMo_9W_3O_{40}$@rht-MOF-1. *Chem. Eng. J.* **2021**, *16*(21), 3363–3370.

(3) Nouar, F.; Eubank, J. F.; Bousquet, T.; Wojtas, L.; Zaworotko, M. J.; Eddaoudi, M. Supermolecular Building Blocks (SBBs) for the Design and Synthesis of Highly Porous Metal-Organic Frameworks. *J. Am. Chem. Soc.* **2008**, *130* (6), 1833–1835.

(4) Ravel, B.; Newville, M. ATHENA, ARTEMIS, HEPHAESTUS: Data Analysis for X-Ray Absorption Spectroscopy Using IFEFFIT. *J. Synchrotron Rad.* **2005**, *12*, 537–541.

(5) Liu, Y.; Sun, J.; Huang, H.; Bai, L.; Zhao, X.; Qu, B.; Xiong, L.; Bai, F.; Tang, J.; Jing, L. Improving CO_2 Photoconversion with Ionic Liquid and Co Single Atoms. *Nat. Commun.* **2023**, *14*, 1457.

(6) Hohenberg, P.; Kohn, W. Inhomogeneous Electron Gas. *Phys. Rev.* **1964**, *136*, B864–B871.

(7) Kohn, W.; Sham, L. J. Self-Consistent Equations Including Exchange and Correlation Effects. *Phys. Rev.* **1965**, *140*, A1133–A1138.

(8) Kresse, G.; Furthmüller, J. Efficient Iterative Schemes for Ab Initio Total-Energy Calculations

(9) Using a Plane-Wave Basis Set. *Phys. Rev. B* **1996**, *54*, 11169.

Blöchl, P. E. Projector Augmented-Wave Method. *Phys. Rev. B* **1994**, *50*, 17953–17979.

(10) Perdew, J. P.; Burke, K.; Ernzerhof, M. Generalized Gradient Approximation Made Simple. *Phys. Rev. Lett.* **1996**, *77*, 3865.

(11) Grimme, S.; Antony, J.; Ehrlich, S.; Krieg, H. A Consistent and Accurate Ab Initio Parametrization of Density Functional Dispersion Correction (DFT-D) for the 94 Elements H–Pu. *J. Chem. Phys.* **2010**, *132*, 154104.

(12) Wagoner, G. Spin Resonance of Charge Carriers in Graphite. *Phys. Rev.* **1960**, *118*, 647–653.

(13) Dyson, F. J. Electron Spin Resonance Absorption in Metals. II. Theory of Electron Diffusion and the Skin Effect. *Phys. Rev.* **1955**, *98*, 349–359.

(14) Funke, H.; Scheinost, A. C.; Chukalina, M. Wavelet Analysis of Extended X-Ray Absorption Fine Structure Data. *Phys. Rev. B* **2005**, *71*, 094110.

(15) Funke, H.; Chukalina, M.; Scheinost, A. C. A New FEFF-Based Wavelet for EXAFS Data Analysis. *J. Synchrotron Radiat.* **2007**, *14*, 426–432.
(16) Zhao, Z.; Zou, Y.; Liu, P.; Lai, Z.; Wen, L.; Jin, Y. EIS Equivalent Circuit Model Prediction Using Interpretable Machine Learning and Parameter Identification Using Global Optimization Algorithms. *Electrochim. Acta* **2022**, *418*, 140350.